

Quantitative models for excess carrier diffusion and recombination in STEM-EBIC experiments on semiconductor nanostructures

T. Meyer,^{1,2} C. Flathmann,^{1,3} D.A. Ehrlich,¹ P. Paap-Peretzki,¹ J. Lindner,² C. Jooß,² and M. Seibt¹

¹4th Institute of Physics –Solids and Nanostructures,

Georg-August-University Goettingen, Friedrich-Hund-Platz 1, Göttingen 37077, Germany

²Institute of Materials Physics, Georg-August-University Goettingen,

Friedrich-Hund-Platz 1, Göttingen 37077, Germany*

³Research Center Future Energy Materials and Systems,

Ruhr University Bochum, Universitätsstr. 150, Bochum 44801, Germany

Faculty of Physics and Astronomy, Ruhr University Bochum, Universitätsstr. 150, Bochum 44801, Germany

(Dated: February 17, 2026)

The increased complexity and reduced size of (opto-)electronic devices demands for quantitative descriptions of excess carrier transport and recombination via various mechanisms. In addition, experimental methods capable of resolving carrier dynamics on the nanometer scale are required. In this paper, we present a quantitative model of a confined geometry including recombination at two surfaces, which is very generic for electron beam induced current measurements in a scanning transmission electron microscope – a method which offers atomic scale spatial resolution. The model is based on analytical considerations as well as finite element simulations and underlying assumptions are subjected to an in-depth discussion. Finally, the successfull application to experimental data obtained on the complex oxide $\text{SrTi}_{0.995}\text{Nb}_{0.005}\text{O}_3$ demonstrates the practicality and robustness of the approach, which enables the precise determination of its bulk diffusion length of $L = 10.2 \pm 0.1 \text{ nm}$.

I. INTRODUCTION

Designing and understanding the functionality of nanometer scale devices is key to several (opto-)electronic applications. Examples include solar to electric energy conversion in ultrathin photovoltaic devices [1], light emission from nitride quantum wells [2], or – among other fascinating fundamental effects – photon detection in two-dimensional transition metal dichalcogenides [3]. Recently, metal halide perovskites gained particular interest due to their potential application in thin film solar cells [4] and light-emitting diodes [5], although, improving their stability [6] and avoiding usage of lead [7, 8] remain major challenges.

Fundamentally, one can separate the optimization of related functional devices into (i) challenges that arise due to bulk properties and (ii) those related to device architectures. A prototypical example for (i) in the context solar cells is given by the prominent Shockley-Queisser limit [9] yielding a material-specific maximal value for the power conversion efficiency. Aligned with the approach of studying single material properties, the effect of bulk defects on photovoltaic performance was studied in classical semiconductors [10] as well as halide perovskites [11]. Furthermore, systems like transition metal oxides in which hot charge carriers can be harvested were studied and hypothesized to exhibit carrier stabilization due to charge [12] and orbital ordering [13]. Concerning aspect (ii), extensive efforts were made to improve the behavior of surfaces and interfaces inevitably included in functional devices: While the surface recombination velocity of solar cells was drastically reduced by passivation [14], the recombination at contact interfaces was optimized by reducing the contact area [15] and adding passivation as well as carrier selective layers [16, 17].

Besides testing the overall performance of macroscopic devices, several microscopic (photo-)electrical characterization methods are available including surface probe techniques like Kelvin probe force microscopy [18], scanning capacitance microscopy [19], or scanning spreading resistance microscopy [20]. Furthermore, photon probes are employed during photoluminescence [21] and light/laser beam induced current [22] measurements as well as electron probes in their respective counterparts called cathodoluminescence [23] and electron beam induced current (EBIC) [24]. The latter – classically conducted in a scanning electron microscope (SEM-EBIC) – combines high spatial resolution and relatively straight-forward interpretation of the signal as excess charge carrier collection efficiency with the possibility of tuning the electron beam energy and thus the contribution of bulk and surface effects.

Based on the analytical solutions found in [25] for the excess charge carrier concentration in a neutral semiconductor terminated by an uncharged surface, several strategies were developed to disentangle the effect of bulk and surface

* tmeyer@uni-goettingen.de

recombination: Accounting for the interaction volume of the electron beam with the sample and tailored geometries used in SEM-EBIC experiments, relations between experimentally observed profile decay lengths and the bulk diffusion length were reported [26–29]. Furthermore, expressions for point generations at a certain depth [30] or close to the surface [31, 32] were suggested and numerical evaluation of infinite series [33] and random walk on spheres based stochastic simulations [34] were used to calculate excess charge carrier collection efficiency profiles.

To further improve the spatial resolution – limited by the electron interaction volume in SEM-EBIC – electron transparent samples were prepared and successfully investigated using scanning transmission electron microscopy (STEM) in [35]. Owing to the small lateral extent of the electron beam, atomically resolved signals can be obtained [36] and several nanostructures were successfully investigated using STEM-EBIC including complex oxide and gallium arsenide heterojunctions [37, 38], silicon homojunctions [39, 40], as well as halide perovskite thin films [41]. Importantly, the same experimental setup can be employed to measure currents induced by the emission of secondary electrons (SE), which is also referred to as SEEBIC, yields atomic scale signals as well [42, 43], and can be used for local thermometry [44] or visualization of nanoparticle morphologies [45]. However, the SE signal is much smaller than currents produced by excess charge carriers and thus contributes only to a small background in STEM-EBIC profiles across rectifying junctions.

In this paper, we combine analytical considerations with numerical simulations using the finite element method (FEM) to establish a quantitative formalism describing the interplay of diffusion as well as bulk and surface recombination of excess charge carriers in a finite, electron transparent semiconductor after a stripe-shaped generation. This enables us to measure nanometer bulk diffusion lengths in STEM-EBIC experiments. The established formalism is applied to experimental data obtained on the complex oxide $\text{SrTi}_{0.995}\text{Nb}_{0.005}\text{O}_3$ yielding a value of $10.2 \pm 0.1 \text{ nm}$ and the model assumptions as well as possible extensions are carefully discussed.

II. RESULTS AND DISCUSSION

Two different geometries are modeled in this study to investigate the effect of surface recombination in electron transparent samples: Firstly, a homogeneous n-type semiconductor of thickness t , in which a stripe generation of excess charge carriers along the z -direction is assumed as shown in Figure 1a. Secondly, a pn junction as illustrated in Figure 1c resulting in a short circuit current through metallic contacts at the semiconductor edges, i.e., a STEM-EBIC signal. In both cases, it is assumed that the materials consist of active interior regions with thickness t_a as well as electronically inactive surface layers with thickness t_d . The latter are also referred to as dead layers and were reported before in the context of electron holography [46, 47] as well as STEM-EBIC [48] to explain vanishing experimental signals at finite sample thicknesses. A more detailed discussion about their possible microscopic nature is given later and surface recombination is assumed to occur at the interface between active and dead layers. The homogeneous geometry in Figure 1a is used to study the total number of excess holes caused by the electron beam as well as decay lengths in excess hole concentration profiles integrated along the z axis as shown in Figure 1b. Obtained formalisms can analogously be applied to excess electrons in p-type semiconductors as well. In addition, the pn junction presented in Figure 1c is evaluated for varying electron beam positions to determine the decay length in the neutral semiconductor region of STEM-EBIC profiles as shown in Figure 1d. The results are structured in three subsections containing analytical considerations, numerical findings, and the application of resulting models to experimental data.

A. Analytical description of excess charge carriers and effective diffusion lengths

The interplay of electrons, holes, and the electrostatic potential in a doped semiconductor is described by the van-Roosbroeck set of differential equations [49]:

$$-\vec{\nabla} \left(\epsilon_0 \epsilon_r \vec{\nabla} \phi \right) = e (N_d - N_a + p - n) , \quad (1)$$

$$0 = \dot{n} = -\vec{\nabla} \left(\mu_e n \vec{\nabla} \phi - D_e \vec{\nabla} n \right) + g - r , \quad (2)$$

$$0 = \dot{p} = -\vec{\nabla} \left(-\mu_h p \vec{\nabla} \phi - D_h \vec{\nabla} p \right) + g - r . \quad (3)$$

Here, n and p are the electron and hole concentrations, ϕ is the electrostatic potential, ϵ_0 and ϵ_r are the vacuum and relative permittivity, N_d and N_a are the concentrations of ionized donor and acceptor dopants, μ_e and μ_h are the electron and hole mobilities, D_e and D_h are the electron and hole diffusivities, g and r are the generation and

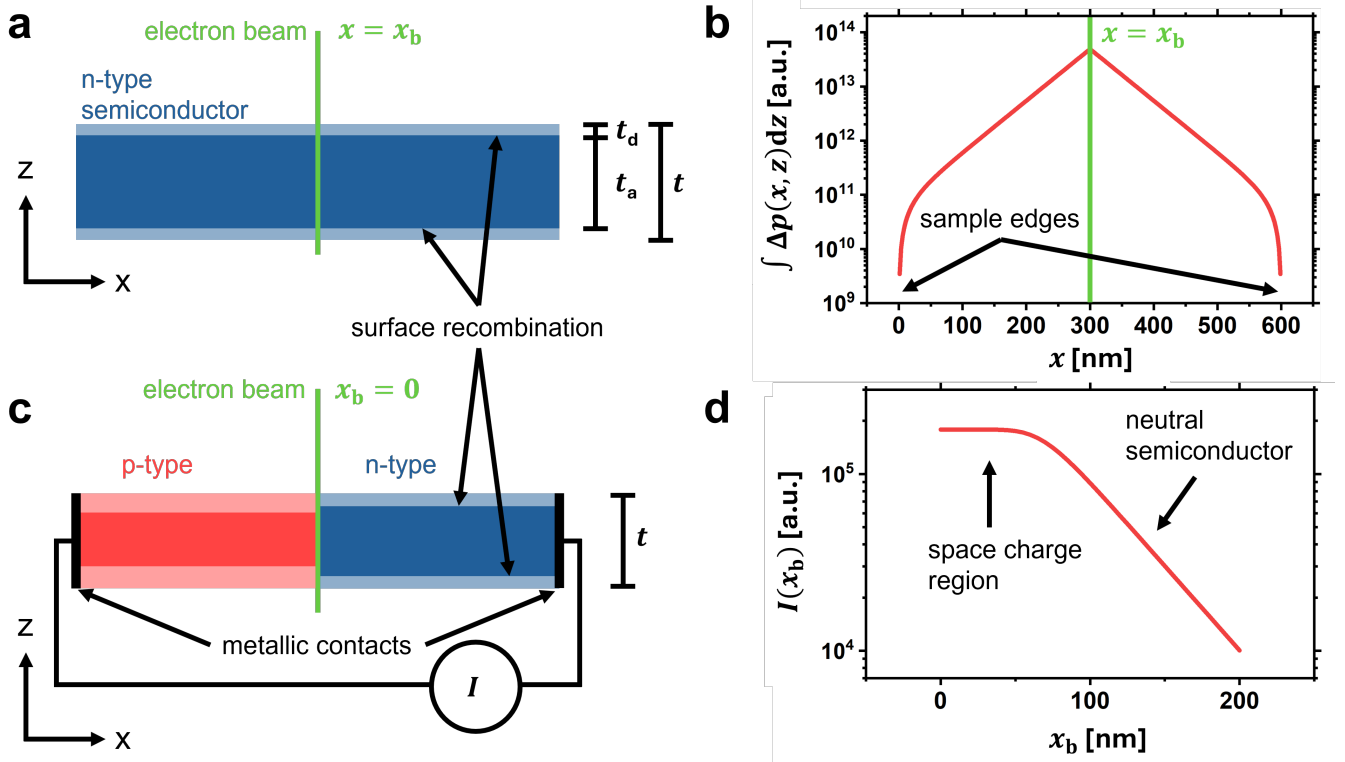


FIG. 1. Overview of modeled geometries: (a) A neutral n-type semiconductor of finite thickness t is excited by a high-energy electron beam causing a stripe shaped generation of excess charge carriers. The material consists of an active interior area with thickness t_a and dead surface layers with thickness t_d and surface recombination occurs at the edges of the active layer. (b) Resulting profile of the excess hole concentration Δp integrated along the z axis. Deviations from an exponential decay at the sample edges are caused by the boundary condition $\Delta p = 0$. (c) Extended geometry including a junction to a p-type semiconductor (with possibly different dead layer thickness) and metallic contacts to probe the short-circuit current caused by the electron beam, i.e., the STEM-EBIC signal. (d) Resulting STEM-EBIC profile with beam positions located in the neutral and space charge region of the n-type material.

recombination functions (being equal for electrons and holes). Setting the time derivatives \dot{n} and \dot{p} to zero corresponds to the stationary case.

The effect of enhanced excess charge carrier recombination due to a surface defect level can be modeled including a Shockley-Read-Hall recombination term for all surface positions [50]:

$$\hat{n} \cdot D \vec{\nabla} p = s \frac{np - n_i^2}{n + n_1 + p + p_1}. \quad (4)$$

Here, \hat{n} is the surface normal vector, s the surface recombination velocity, n_i the intrinsic charge carrier concentration and the electron and hole concentrations n_1 and p_1 correspond to the values expected if the electrochemical potential is located at the defect level. Furthermore, $D = (n_{\text{eq}} + p_{\text{eq}})/(n_{\text{eq}}/D_h + p_{\text{eq}}/D_e)$ is the ambipolar diffusivity related to the equilibrium concentrations of electrons n_{eq} and holes p_{eq} . In case of an n-type material ($n \gg p$), weak injection ($n \approx n_{\text{eq}}$), and a deep level defect ($n \gg n_1 + p_1$), Equation (4) can be approximated as

$$\hat{n} \cdot D \vec{\nabla} p \approx s \Delta p, \quad (5)$$

with the excess charge carrier concentration $\Delta p = p - p_{\text{eq}}$.

A general solution of Equations (1)-(3) for arbitrary geometries remains elusive, however, simplified cases can be evaluated analytically: In [25], a field-free, single material n-type semiconductor was considered in a semi-infinite geometry including point, stripe, and planar generation functions and explicit expressions for the excess hole concentrations was found using Green's functions. Based on these results, the total number of excess holes in the semi-infinite

case and for a point generation with generation function $g = G\delta(x, y, z - \xi)$ was found in [30] to be:

$$\Delta p_{\text{semi-inf}}^{\text{tot}}(\xi) = \frac{GL^2}{D} \left(1 - \frac{s}{s+1} \exp(-\xi/L) \right) = \Delta p_{\infty}^{\text{tot}} \left(1 - \frac{s}{s+1} \exp(-\xi/L) \right). \quad (6)$$

Here, G denotes the generation strength, L the bulk diffusion length for holes, and ξ the generation distance from the surface. Furthermore, $\Delta p_{\infty}^{\text{tot}} = GL^2/D$ corresponds to the total number of excess holes for a recombination-free surface (or an infinite semiconductor). We emphasize that $\Delta p_{\text{semi-inf}}^{\text{tot}}$ and $\Delta p_{\infty}^{\text{tot}}$ – obtained by integrating the excess hole concentration over all spatial coordinates – are dimensionless.

By accounting for a second surface with an additional reduction term in Equation (6) and an adopted boundary condition analogous to Equation (5) as shown in [51], an analytical expression for the total number of excess holes can be derived for a finite geometry with (active) thickness $t_a = t - 2t_d$. Averaging the result for all generation depths contained in the active sample region, i.e., assuming a stripe generation of excess charge carriers yields the following expression:

$$\Delta p^{\text{tot}} = \Delta p_{\infty}^{\text{tot}} \left(1 - \frac{\frac{2L}{t_a}}{\frac{D}{sL} + \coth\left(\frac{t_a}{2L}\right)} \right), \quad t_a = t - 2t_d. \quad (7)$$

Following the approach in [30] to define a global, effective lifetime satisfying $\tau^{\text{eff}}/\tau = \Delta p^{\text{tot}}/\Delta p_{\infty}^{\text{tot}}$ (with τ being the bulk lifetime) leads to an effective diffusion length of

$$L_{\tau}^{\text{eff}} = \sqrt{D\tau^{\text{eff}}} = L \cdot \sqrt{1 - \frac{\frac{2L}{t_a}}{\frac{D}{sL} + \coth\left(\frac{t_a}{2L}\right)}}, \quad t_a = t - 2t_d. \quad (8)$$

The subscript τ indicates that the effective diffusion length was calculated via the effective lifetime.

We emphasize that the validity of both the ansatz for an additional surface term leading to Equation (7) as well as the assumption that a global effective lifetime can be used to derive Equation (8) remains unclear at this point and will be investigated in the following sections, while Equation (6) is a direct consequence of the solutions presented in [25].

B. Numerical simulation results and an empirical correction

To check the validity of Equation (7) and (8), the two geometries in Figure 1a and 1c are modeled numerically and Equations (1)-(3) are solved via FEM using the surface recombination term given in Equation (4). A midgap defect level is assumed, i.e., the defect level is set to the center of the band gap, and the inactive, dead layers are omitted in the numerical model. More details about the simulation parameters and boundary conditions are given in the supporting information. Exemplary profiles of resulting excess hole concentrations and STEM-EBIC signals were already presented in Figure 1b and 1d and exhibit following behavior: The excess hole concentration profile decays exponentially with increasing distance from the electron beam position (except in the vicinity of the sample edges, where $\Delta p = 0$ is enforced by the boundary conditions). The STEM-EBIC profile, however, decays only exponentially in the neutral semiconductor region (and well-separated from the contacts), while a saturation is observed in the space charge region involving finite electric fields. We emphasize that depending on the recombination mechanisms and electric field strength, sharp maxima can be observed in the space charge region as well, which is the case for the experimental data shown in the following subsection. To reliably extract the related decay lengths, a tailored criterion to objectively define a suitable fitting regime excluding space charge region and edge effects is used, which is described in detail in the supporting information. The decay length obtained from the excess hole concentration is denoted by $L_{\Delta p}$ and the decay length of STEM-EBIC profiles by L_I .

The resulting values for Δp^{tot} , $L_{\Delta p}$, and L_I are plotted as points in Figure 2 for different thicknesses and surface recombination velocities enabling a comparison to the analytical equations included as lines: In fact, the FEM results of Δp^{tot} in Figure 2a perfectly agree with Equation (7) proving that the additional surface term used to derive it from the semi-infinite case correctly models the finite geometry. Furthermore, Δp^{tot} decreases as expected monotonously with increasing s or decreasing t_a . Qualitatively, the same trend is visible for the two decay lengths $L_{\Delta p}$ (points) and L_I (crosses) in Figure 2b, which are virtually identical. Importantly, the observation $L_{\Delta p} = L_I$ confirms that STEM-EBIC profiles in a neutral, extrinsic semiconductor directly probe the excess carrier diffusion and justifies the definition of a single effective diffusion length by the common value. A quantitative match between the simulation results with Equation (8) (dashed lines), however, is only observed for small values of s or t_a . Thus, considering the

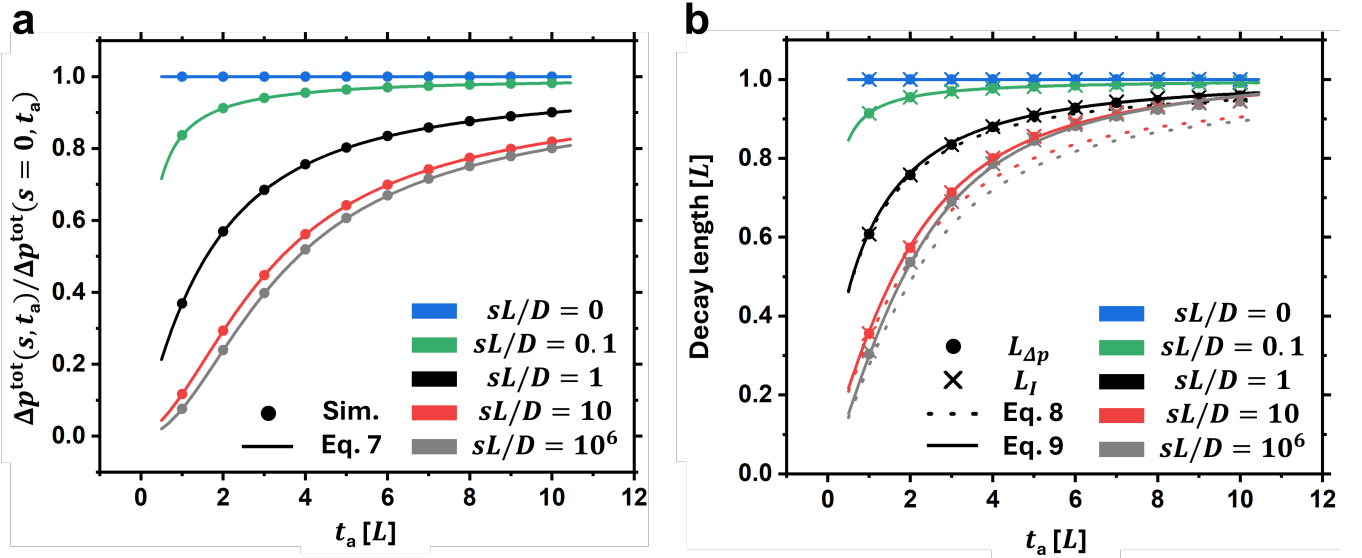


FIG. 2. Comparison between numerical simulation results and model equations for different values of the surface recombination velocity s as a function of active thickness t_a : (a) shows the total number of excess holes Δp^{tot} obtained via FEM for the geometry in Figure 1a (points) and the analytical prediction by Equation (7) (lines). (b) shows the decay lengths $L_{\Delta p}$ and L_I obtained from exponential fits of the excess hole concentration integrated along z (points, model shown in Figure 1a) as well as the STEM-EBIC profiles (crosses, model shown in Figure 1c). In addition, the predictions by Equations (8) and (9) are shown as dashed and solid lines.

total number of excess charge carriers and effective diffusion lengths leads to different values of corresponding effective lifetimes, which were assumed to be identical when deriving Equation (8) from (7). Lacking an analytical solution, we propose an empirical correction accounting for the systematic underestimation of the effective diffusion length by Equation (8), which is given by the following expression:

$$L_{\text{emp}}^{\text{eff}} = L_{\tau}^{\text{eff}} + 0.0666 \cdot \frac{\left(\frac{t_a}{L}\right)^2}{1 + \frac{t_a}{L}} \cdot \frac{\frac{sL}{D}}{1 + \frac{sL}{D}} \cdot (L - L_{\tau}^{\text{eff}}), \quad t_a = t - 2t_d. \quad (9)$$

The last factor of the correction term $L - L_{\tau}^{\text{eff}}$ is motivated by the fact that all data points in Figure 2b are located between L and L_{τ}^{eff} , while the two central terms are chosen to guarantee that the correction term vanishes for small values of s or t_a . The quadratic dependence of t_a/L in the nominator of the second term is found to describe the data points slightly better than a linear term and the prefactor of 0.0666 is found by minimizing the mean square difference between simulated results and Equation (9). Importantly, spot-checked changes of the used numerical parameters such as mesh and model sizes, the defect energy level, the bulk recombination parameter, doping levels, or mobilities lead to results identical to those in Figure 2 implying that the empirically found prefactor does not depend on material properties, but reflects the underlying geometry. Even though the empirical solution is not derived mathematically, its high accuracy in describing the results obtained in the FEM simulations across the entire range of relevant values for s and t_a suggests, that it can be readily used to extract quantitative values for L and s in STEM-EBIC experiments.

C. Experimental quantification of bulk diffusion lengths and surface recombination velocities

In this section, the formalisms presented in the previous two subsections are applied to experimental data obtained on a heterojunction formed by a Ruddlesden-Popper $\text{Pr}_{0.5}\text{Ca}_{1.5}\text{MnO}_4$ (RP-PCMO) thin film on a $\text{SrTi}_{0.995}\text{Nb}_{0.005}\text{O}_3$ (STNO) substrate. The thin film is grown by ion beam sputtering and an electron transparent sample is extracted using focused ion beam (FIB). More details about the macroscopic and TEM sample preparation are given in the experimental section and an SEM overview of the final lamella is shown in Figure 3a. Importantly, the latter is thinned in a wedge shape such that an intentional thickness gradient is present from left to right. The current-voltage characteristic of the TEM lamella shows strong rectifying behavior and is perfectly consistent with the data obtained on the macroscopic sample as demonstrated in Figure 3b. To investigate the thickness dependence of STEM-EBIC signals across the heterojunction, vertical profiles are collected in the region marked by the yellow rectangle in the

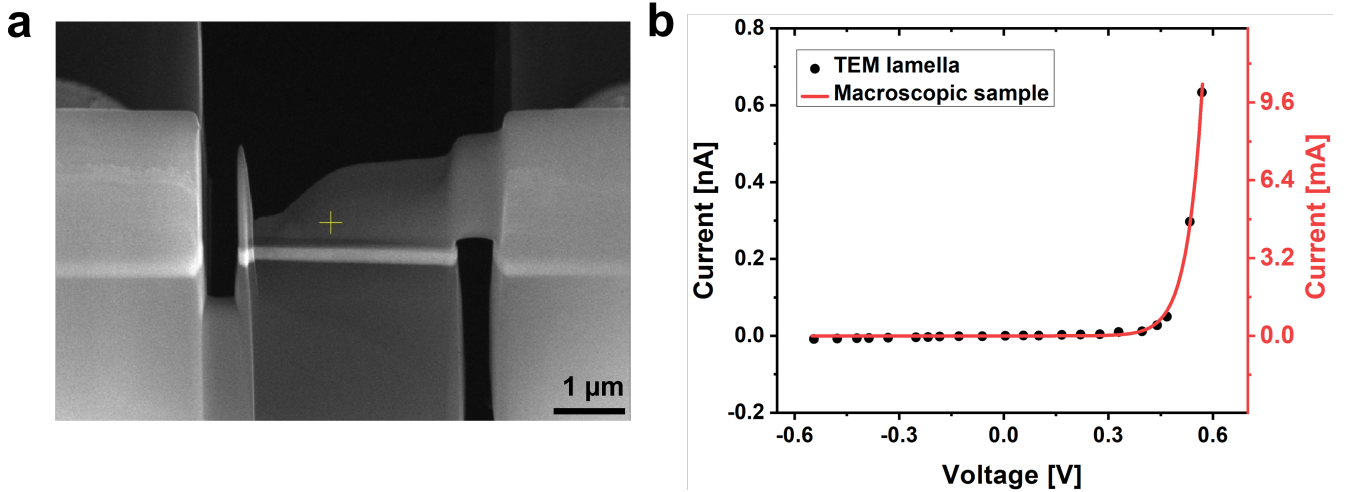


FIG. 3. (a) SEM overview of the lamella extracted from an RP-PCMO-STNO junction and mounted on a MEMS chip. Vertical cuts were applied to prevent short circuits across the junction. (b) Comparison of the current-voltage characteristics of the lamella (black points) and the macroscopic sample (red line).

annular dark-field STEM image in Figure 4a. Due to the wedge shape of the lamella, different horizontal positions correspond to different local thicknesses and details how the latter is determined using electron energy loss spectroscopy (EELS) are given in the supporting information. Three exemplary profiles marked by arrows in Figure 4a are plotted in Figure 4b showing clear STEM-EBIC signals in the vicinity of the junction. As reported previously for related manganite thin films [37, 48], the signal in the RP-PCMO is low due to the short lifetime of excess carriers and thus the discussion will focus on the n-type STNO substrate. Two main observation can be inferred from the profiles: Firstly, the maximum current increases with the sample thickness, which is expected due to the longer interaction path of the electrons leading to more excess carrier generation. Secondly, the increased signal width in the STNO indicates higher effective diffusion lengths for higher thicknesses. For further illustration, the maximal EBIC values as well as the effective diffusion lengths are shown as a function of thickness in Figure 4c+d. The latter are extracted analogously to those from simulated profiles as documented in the supporting information. The maximal EBIC in Figure 4c shows a linear dependence in the investigated thickness regime and the extrapolated linear fit intersects the thickness axis at 30 ± 1 nm. Since the maximum position is obtained in the substrate, this indicates a dead layer thickness of 15.0 ± 0.5 nm for STNO. Furthermore, the effective diffusion length given in Figure 4d increases – as expected – with the thickness and the least-squares model fit to Equation (9) describes the experimental data remarkably well. The obtained fit parameters are $L = 10.2 \pm 0.2$ nm, $s/D = 1.6 \times 10^5 \pm 8 \times 10^{10}$ nm $^{-1}$, and $t_d = 15 \pm 5$ nm. The errors are calculated from the covariance matrix of the least-squares fit and the fact that the value for s/D is five orders of magnitude below its estimated error reflects that the model equation is virtually independent of s/D for the obtained optimal parameters. This finding perfectly aligns with the numerical results in Figure 2 showing that the effective diffusion length hardly changes for values of $sL/D > 10$. Therefore, a second fit assuming the limiting case $s = \infty$ is performed yielding the values $L = 10.2 \pm 0.1$ nm and $t_d = 15.0 \pm 0.3$ nm. Consistently, the values are identical to those obtained including three fit parameters and solely the estimated errors are decreased. Remarkably, the value for the dead layer thickness equals that one extracted from the intersect of the EBIC maximum in Figure 4c underlining the model's overall accuracy.

III. CONCLUSION AND OUTLOOK

Quantitative modeling of excess charge carrier dynamics in confined semiconductor geometries is of high relevance to describe non-equilibrium states in (opto-)electronic devices. In this paper, analytical expressions describing a thin, electron transparent sample and including surface recombination were revised and tested by finite element simulations as well as experimental data resulting in a quantitative match and successful determination of the bulk diffusion length $L = 10.2 \pm 0.1$ nm for $\text{SrTi}_{0.995}\text{Nb}_{0.005}\text{O}_3$. Furthermore, it was shown that the surface recombination velocity is virtually infinity after FIB preparation and dead layers with a thickness of $t_d = 15.0 \pm 0.3$ nm reduce the effective sample thickness in STEM-EBIC experiments.

The presented findings have several important implications related to semiconductor modeling in general as well as

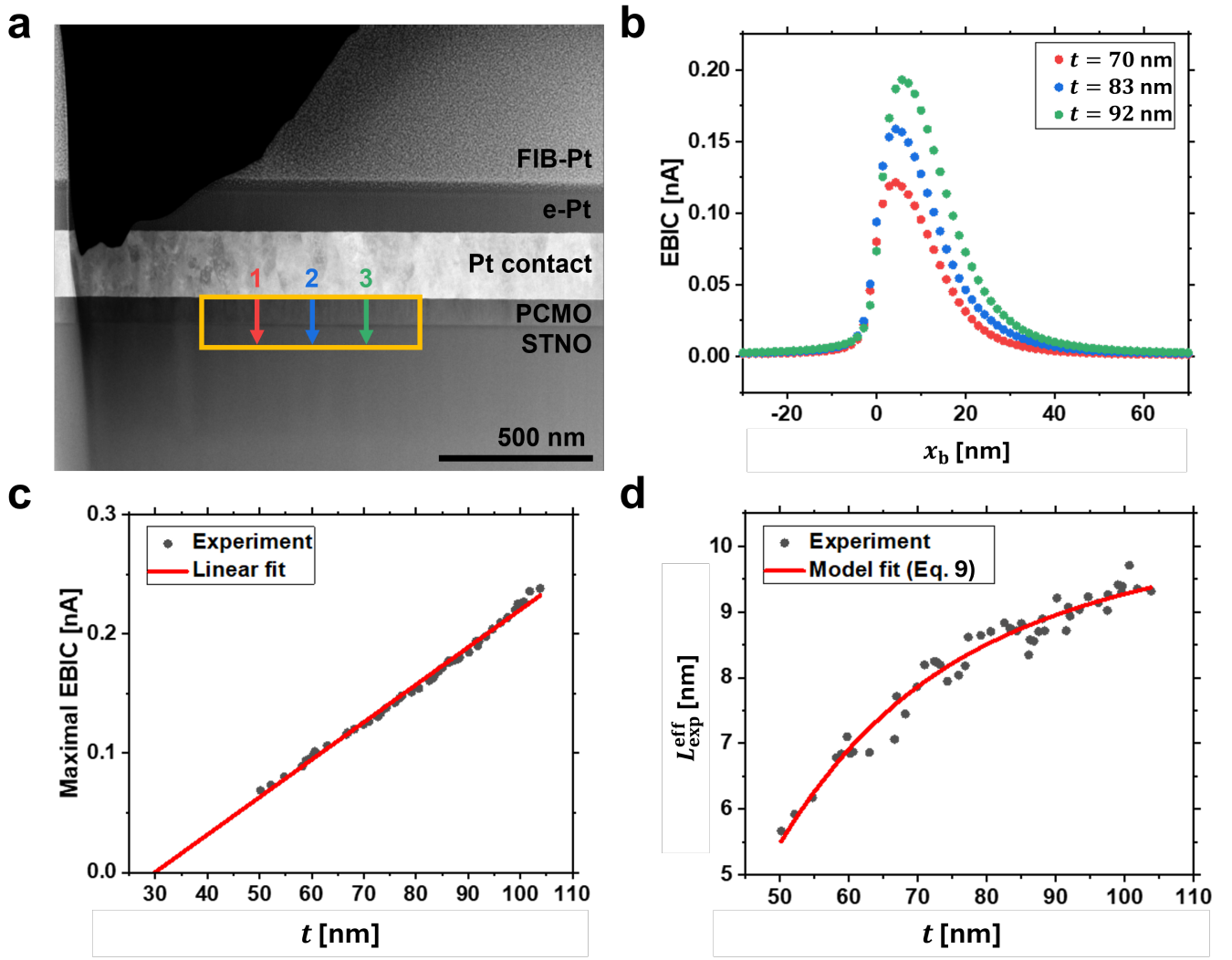


FIG. 4. (a) Annular dark-field STEM image showing all layers of the junction and the front contact. The region marked by the yellow rectangle was analyzed with vertical STEM-EBIC scans and contains an intentional thickness gradient in the horizontal direction. The three arrows indicate the profiles along which the current is shown in (b). (c) and (d) show the thickness dependence of the line profiles' maximal STEM-EBIC signal and decay length in the n-type STNO substrate (points). While (c) includes a linear regression of the data points, a model fit to Equation (9) is given in (d) (lines).

EBIC experiments in particular: Firstly and most importantly, the results clearly define suitable strategies to extract bulk diffusion lengths on the order of several nanometers to a few hundred nanometers with STEM-EBIC: For values up to a few tens of nanometers, a constant sample thickness around ten times the bulk diffusion length or higher can be used leading to deviations of the effective value by less than 10 %. In contrast, for larger values, the thickness-dependent approach applied in this paper can be used to extrapolate the value of the bulk diffusion length or – if the spatial resolution is sufficient – SEM-EBIC can be employed. Secondly, we have shown that an analytical expression for the total number of excess charge carriers Δp^{tot} can be obtained by incorporating several reduction terms each corresponding to individual surfaces. This concept might be transferrable to more complex geometries like faceted nanowires or quantum dots. Lastly, the perfect match between the resulting three-dimensional analytical description of Δp^{tot} and the two-dimensional simulation results implies that a reduction of the dimensionality of translational invariant geometries is generally justified. The approach to reduce the dimensionality was taken further by introducing an effective diffusion length and thus an effectively one-dimensional description of STEM-EBIC profiles in the neutral semiconductor region. Importantly, the latter could not be achieved by using the effective carrier lifetime deduced from the total number of excess carriers as previously assumed in [30], but required an empirical correction backed by the FEM simulations.

Future work should focus on formalisms including surface charges or the electric field inside the space charge region. The former are expected to be strongly linked to the dead layers observed in experiments and the latter could be addressed experimentally by mapping the electric field with electron holography [52–55] or four-dimensional STEM [56–59] – methods that can also be used to correlate the observed electronic properties with phase transitions related to long-living hot carriers [60, 61]. Furthermore, an analytical explanation of the used empirical correction is desirable.

In short, we have demonstrated for the first time how nanometer scale diffusion lengths can be precisely determined using STEM-EBIC and the concepts used in this paper will largely help to establish quantitative models describing excess charge carrier dynamics in nanoscale (opto-)electronic devices.

IV. EXPERIMENTAL SECTION

A. Finite element simulations

Two-dimensional finite element simulations were conducted with COMSOL Multiphysics v6.1.0.357 using a stationary solver and including the electric potential as well as the electron and hole concentrations as variables. The minimal and maximal mesh size was set to 0.02 nm and 2 nm and all relevant parameters, used boundary conditions, and the definition of the STEM-EBIC probe are given in the supporting information.

B. Macroscopic sample preparation

An 80 nm thick $\text{Pr}_{0.5}\text{Ca}_{1.5}\text{MnO}_4$ film was epitaxially grown on a single-crystalline, double-side-polished, (110)-oriented $\text{SrTi}_{0.995}\text{Nb}_{0.005}\text{O}_3$ substrate via ion beam sputtering using pressures of $p_{\text{Ar}} = 3 \times 10^{-4}$ mbar (beam neutralizer), $p_{\text{Xe}} = 1 \times 10^{-4}$ mbar (sputter gas), and $p_{\text{O}} = 1.4 \times 10^{-4}$ mbar (film oxidation) during deposition. The boron nitride heater was set to 790 °C, which corresponds approximately to 700 °C at the substrate surface and a cooling rate of 10 °C/min with 20 min holding steps at 690, 490, and 290 °C was used after deposition.

C. Focussed ion beam preparation

TEM samples were prepared in a Thermo Fisher Scientific Helios G4 gallium FIB. Electron and FIB deposited platinum was used to form a conductive protection bar on the surface of the sputtered platinum front contact. A cross-sectional slice was transferred to a DENSSolutions MEMS chip including two biasing and four heating contacts. After mounting on the chip, FIB platinum was used for electrical contacting of the STNO substrate as well as the front contact to the biasing contacts and vertical cuts were milled to avoid short circuits of the rectifying junction. The front and rear thinning patterns were rotated by 5° to create a wedge-shaped sample and the acceleration voltage during final ion polishing was set to 2 kV.

D. Transmission electron microscopy

STEM-EBIC experiments were conducted in an FEI Titan 80–300 G2 ETEM operated at 300 kV and using a DENSSolutions Lightning D7+ sample holder. The convergence semi-angle was set to 10 mrad and the beam current to 42 pA. STEM-EBIC currents were converted to a voltage signal with a Stanford Research Systems SR570 current preamplifier and recorded synchronously to annular dark-field signals as well as EELS data using a Gatan Quantum 965 ER image filter including an UltraScan 1000XP CCD camera and a collection semi-angle of 47 mrad. The local sample thickness in the STNO substrate was determined via EELS using the log-ratio method and a mean free path of 149.1 nm as suggested by the parametrization in [62].

Supporting Information

Supporting Information is available from the Wiley Online Library or from the author.

Acknowledgements

The authors thank B. Kressdorf for providing the macroscopic heterojunction sample. This work was financially supported by the Deutsche Forschungsgemeinschaft (DFG, German Research Foundation) 217133147/SFB 1073, projects B02, C02, and project 429413061 (SE560/-1) as well as by the German State of Lower Saxony (FuturePV project). The use of equipment of the “Collaborative Laboratory and User Facility for Electron Microscopy” (CLUE, Göttingen) is gratefully acknowledged.

Author Contributions Statement T.M.: conceptualization; data curation; formal analysis; investigation; methodology; software; validation; visualization; writing—original draft; writing—review & editing. C.F.: formal analysis; investigation; methodology; validation; writing—review & editing. D.A.E.: formal analysis; investigation; methodology; software; validation; writing—review & editing. P.P.-P.: conceptualization; formal analysis; methodology; software; validation; writing—review & editing. J.L.: investigation; methodology; software; writing—review & editing. C.J.: writing—review & editing; resources; supervision; funding acquisition. M.S.: conceptualization; formal analysis; methodology; writing—review & editing; resources; funding acquisition; supervision; project administration.

Data Availability Statement

The data that support the findings of this study are openly available in [63] and additional raw data are available from the corresponding author upon reasonable request.

[1] I. Massiot, A. Cattoni, S. Collin, *Nature Energy* **2020**, *5*, 12 959.

[2] M. Sheen, Y. Ko, D.-u. Kim, J. Kim, J.-h. Byun, Y. Choi, J. Ha, K. Y. Yeon, D. Kim, J. Jung, et al., *Nature* **2022**, *608*, 7921 56.

[3] Q. H. Wang, K. Kalantar-Zadeh, A. Kis, J. N. Coleman, M. S. Strano, *Nature nanotechnology* **2012**, *7*, 11 699.

[4] M. A. Green, A. Ho-Baillie, H. J. Snaith, *Nature photonics* **2014**, *8*, 7 506.

[5] A. Fakharuddin, M. K. Gangishetty, M. Abdi-Jalebi, S.-H. Chin, A. R. bin Mohd Yusoff, D. N. Congreve, W. Tress, F. Deschler, M. Vasilopoulou, H. J. Bolink, *Nature Electronics* **2022**, *5*, 4 203.

[6] F. Du, X. Liu, J. Liao, D. Yu, N. Zhang, Y. Chen, C. Liang, S. Yang, G. Fang, *Advanced Functional Materials* **2024**, *34*, 12 2312175.

[7] T. Miyasaka, A. Kulkarni, G. M. Kim, S. Öz, A. K. Jena, *Advanced Energy Materials* **2020**, *10*, 13 1902500.

[8] S. Hoffmann-Urlaub, Y. Zhang, Z. Wang, B. Kressdorf, T. Meyer, *Applied Physics A* **2020**, *126*, 7 553.

[9] W. Shockley, H. Queisser, *J Appl Phys* **32** 510.

[10] H. J. Queisser, E. E. Haller, *Science* **1998**, *281*, 5379 945.

[11] J. M. Ball, A. Petrozza, *Nature Energy* **2016**, *1*, 11 1.

[12] B. Kressdorf, T. Meyer, A. Belenchuk, O. Shapoval, M. Ten Brink, S. Melles, U. Ross, J. Hoffmann, V. Moshnyaga, M. Seibt, et al., *Physical Review Applied* **2020**, *14*, 5 054006.

[13] B. Kressdorf, T. Meyer, M. Ten Brink, C. Seick, S. Melles, N. Ottinger, T. Titze, H. Meer, A. Weisser, J. Hoffmann, et al., *Physical Review B* **2021**, *103*, 23 235122.

[14] J. Schmidt, R. Peibst, R. Brendel, *Solar Energy Materials and Solar Cells* **2018**, *187* 39.

[15] A. Blakers, *IEEE Journal of Photovoltaics* **2019**, *9*, 3 629.

[16] V. Titova, J. Schmidt, *AIP Advances* **2018**, *8*, 12.

[17] C. Flathmann, T. Meyer, V. Titova, J. Schmidt, M. Seibt, *Scientific Reports* **2023**, *13*, 1 3124.

[18] M. Vishwakarma, D. Varandani, C. Andres, Y. E. Romanyuk, S. G. Haass, A. N. Tiwari, B. R. Mehta, *Solar Energy Materials and Solar Cells* **2018**, *183* 34.

[19] K. Matsumura, T. Fujita, H. Itoh, D. Fujita, *Measurement Science and Technology* **2014**, *25*, 4 044020.

[20] P. Eyben, F. Seidel, T. Hantschel, A. Schulze, A. Lorenz, A. U. De Castro, D. Van Gestel, J. John, J. Horzel, W. Vandervorst, *physica status solidi (a)* **2011**, *208*, 3 596.

[21] T. Trupke, B. Mitchell, J. Weber, W. McMillan, R. Bardos, R. Kroese, *Energy Procedia* **2012**, *15* 135.

[22] B. Moralejo, M. González, J. Jiménez, V. Parra, O. Martínez, J. Gutiérrez, O. Charro, *Journal of electronic materials* **2010**, *39*, 6 663.

[23] T. Coenen, N. Haegel, *Applied Physics Reviews* **2017**, *4*, 3.

[24] H. Leamy, *Journal of Applied Physics* **1982**, *53*, 6 R51.

[25] W. Van Roosbroeck, *Journal of Applied Physics* **1955**, *26*, 4 380.

[26] W. Hackett Jr, *Journal of Applied Physics* **1972**, *43*, 4 1649.

[27] C. Donolato, *Applied Physics Letters* **1983**, *43*, 1 120.

[28] C. Donolato, *Applied Physics Letters* **1999**, *75*, 25 4004.

[29] K. L. Luke, O. von Roos, L.-j. Cheng, *Journal of applied physics* **1985**, *57*, 6 1978.

[30] L. Jastrzebski, J. Lagowski, H. Gatos, *Applied Physics Letters* **1975**, *27*, 10 537.

[31] F. Berz, H. Kuiken, *Solid-State Electronics* **1976**, *19*, 6 437.

[32] V. Ong, J. Phang, D. Chan, *Solid-state electronics* **1994**, *37*, 1 1.

[33] C. C. Tan, V. K. Ong, K. Radhakrishnan, *Progress in Photovoltaics: Research and Applications* **2013**, *21*, 5 986.

[34] I. Shalimova, K. K. Sabelfeld, *Monte Carlo Methods and Applications* **2018**, *24*, 1 43.

[35] C. Cabanel, D. Brouri, J. Laval, *The European Physical Journal-Applied Physics* **2006**, *34*, 2 107.

[36] T. Meyer, et al., Ph.D. thesis, PhD thesis, Dissertation, Göttingen, Georg-August Universität, **2020**.

[37] T. Meyer, B. Kressdorf, J. Lindner, P. Peretzki, V. Roddatis, C. Jooss, M. Seibt, In *Journal of Physics: Conference Series*, volume 1190. IOP Publishing, **2019** 012009.

[38] B. T. Zutter, H. Kim, W. A. Hubbard, D. Ren, M. Mecklenburg, D. Huffaker, B. Regan, *Physical Review Applied* **2021**, *16*, 4 044030.

[39] A. P. Conlan, G. Moldovan, L. Bruas, E. Monroy, D. Cooper, *Journal of Applied Physics* **2021**, *129*, 13.

[40] S. Schneider, S. Beckert, R. Hammer, M. König, G. Moldovan, D. Pohl, *arXiv preprint arXiv:2511.11528* **2025**.

[41] M. Duchamp, H. Hu, Y. M. Lam, R. Dunin-Borkowski, C. B. Boothroyd, *Ultramicroscopy* **2020**, *217* 113047.

[42] M. Mecklenburg, W. A. Hubbard, J. J. Lodico, B. Regan, *Ultramicroscopy* **2019**, *207* 112852.

[43] O. Dyck, J. Almutlaq, D. Lingerfelt, J. L. Swett, M. P. Oxley, B. Huang, A. R. Lupini, D. Englund, S. Jesse, *Nature Communications* **2023**, *14*, 1 7550.

[44] W. A. Hubbard, M. Mecklenburg, H. L. Chan, B. Regan, Emission-based temperature mapping with stem ebic, **2023**.

[45] E. Vlasov, A. Skorikov, A. Sánchez-Iglesias, L. M. Liz-Marzan, J. Verbeeck, S. Bals, *ACS Materials Letters* **2023**, *5*, 7 1916.

[46] W. Rau, P. Schwander, F. Baumann, W. Höppner, A. Ourmazd, *Physical Review Letters* **1999**, *82*, 12 2614.

[47] A. Twitchett, R. Dunin-Borkowski, P. Midgley, *Physical review letters* **2002**, *88*, 23 238302.

[48] P. Peretzki, B. Ifland, C. Jooss, M. Seibt, *physica status solidi (RRL)-Rapid Research Letters* **2017**, *11*, 1 1600358.

[49] W. Van Roosbroeck, *The Bell System Technical Journal* **1950**, *29*, 4 560.

[50] P. M. Haney, H. P. Yoon, B. Gaury, N. B. Zhitenev, *Journal of applied physics* **2016**, *120*, 9.

[51] P. Peretzki, Ph.D. thesis, Niedersächsische Staats-und Universitätsbibliothek Göttingen, **2019**.

[52] S. Anada, T. Hirayama, H. Sasaki, K. Yamamoto, *Journal of Applied Physics* **2020**, *128*, 24.

[53] L. Denaix, F. Castioni, M. Bryan, D. Cooper, E. Monroy, *ACS Applied Materials & Interfaces* **2023**, *15*, 8 11208.

[54] H. Çelik, R. Fuchs, S. Gaebel, C. M. Günther, M. Lehmann, T. Wagner, *Ultramicroscopy* **2024**, *267* 114057.

[55] J. Lindner, U. Ross, T. Meyer, V. Boureau, M. Seibt, C. Jooss, *Ultramicroscopy* **2024**, *256* 113880.

[56] L. Wu, M.-G. Han, Y. Zhu, *Ultramicroscopy* **2023**, *250* 113745.

[57] S. Toyama, T. Seki, Y. Kanitani, Y. Kudo, S. Tomiya, Y. Ikuhara, N. Shibata, *Nature Nanotechnology* **2023**, *18*, 5 521.

[58] A. Wartelle, B. C. da Silva, D. Cooper, M. I. den Hertog, *Journal of Applied Physics* **2025**, *138*, 10.

[59] C. Flathmann, U. Ross, J. Belz, A. Beyer, K. Volz, M. Seibt, T. Meyer, *Microscopy and Microanalysis* **2025**, *31*, 5 ozaf086.

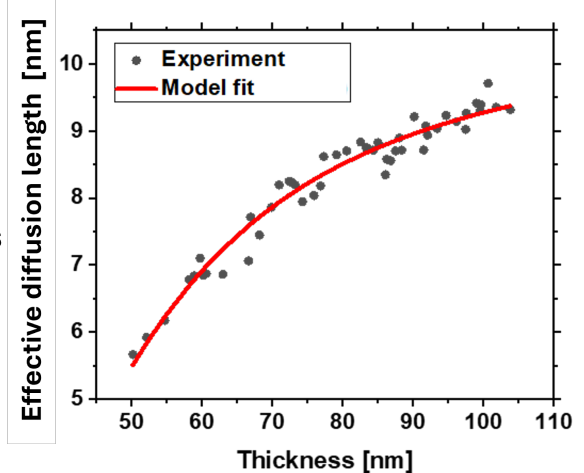
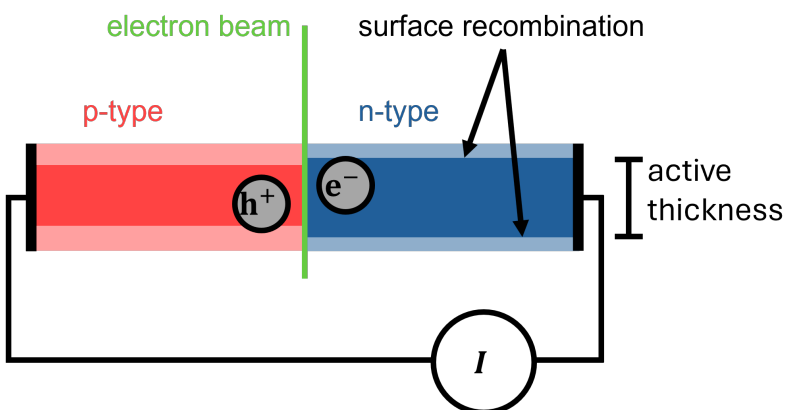
[60] T. Meyer, B. Kressdorf, V. Roddatis, J. Hoffmann, C. Jooss, M. Seibt, *Small Methods* **2021**, *5*, 9 2100464.

[61] C. Flathmann, T. Meyer, U. Ross, A. Dehning, C. Jooss, M. Seibt, *APL Materials* **2024**, *12*, 6.

[62] K. Iakoubovskii, K. Mitsuishi, Y. Nakayama, K. Furuya, *Microscopy research and technique* **2008**, *71*, 8 626.

[63] T. Meyer, C. Flathmann, D. A. Ehrlich, P. Paap-Peretzki, J. Lindner, C. Joob, M. Seibt, Data for: Quantitative modeling of excess charge carrier diffusion and recombination in electron transparent samples, **2026**, URL <https://doi.org/10.25625/IWVEOW>.

Table of Contents



Diffusion and recombination of excess charge carriers in a semiconducting material are considered using a finite geometry that is tailored for electron beam induced current measurements in a scanning transmission electron microscope. A quantitative model is developed based on analytical considerations as well as finite element simulations and applied successfully to experimental data.

Supporting Information to

QUANTITATIVE MODELS FOR EXCESS CARRIER DIFFUSION AND RECOMBINATION IN STEM-EBIC EXPERIMENTS ON SEMICONDUCTOR NANOSTRUCTURES

Details of FEM simulations

The parameters used in the FEM simulations are summarized in Table S1. The boundary conditions corresponding to the boundaries indexed in Figure S1 and using the parameters listed in Table S1 are given in Table S2 and STEM-EBIC currents for the geometry in Figure S1b were evaluated by integrating the total current density j_{tot} at boundary 2 defined by:

$$j_{\text{tot}} = e \left(D_e \vec{\nabla} n - D_h \vec{\nabla} p \right).$$

No significant differences between currents extracted at boundary 2 and 3 were observed.

Table S1: Parameters used in the FEM simulations. If applicable, different values for the p- and n-type material used in the geometry shown in Figure 1a are given in separate columns.

Quantity	Description	n-type material	p-type material
d	Material width	1200 nm	
T	Temperature	300 K	
E_g	Band gap	1.12 eV	
ϵ_r	Relative permittivity	11.9	
μ_e	Electron mobility	1100 cm ² /V/s	
μ_h	Hole mobility	200 cm ² /V/s	
D_e	Electron diffusivity	0.0028437 m ² /s	
D_h	Hole diffusivity	5.1704E-4 m ² /s	
N_d	Donor concentration	0 cm ⁻³	10 ¹⁷ cm ⁻³
N_a	Acceptor concentration	10 ¹⁷ cm ⁻³	0 cm ⁻³
N_C	Conduction band effective DOS	2.5055 × 10 ¹⁷ cm ⁻³	
N_V	Valence band effective DOS	2.5055 × 10 ¹⁷ cm ⁻³	
n_i	Intrinsic charge carrier concentration	9.802 × 10 ⁹ cm ⁻³	
n_1	Mid-gap electron concentration	9.802 × 10 ⁹ cm ⁻³	
p_1	Mid-gap hole concentration	9.802 × 10 ⁹ cm ⁻³	
n_{eq}	Equilibrium electron concentration	10 ¹⁷ cm ⁻³	9.6079 × 10 ² cm ⁻³
p_{eq}	Equilibrium hole concentration	9.6079 × 10 ² cm ⁻³	10 ¹⁷ cm ⁻³
V_{bi}	Built-in potential		0.8344 V
r	Recombination function		$B \cdot (np - n_i^2)$
B	Bulk recombination coefficient		2.5 × 10 ⁻⁶ cm ³ /s
$g(x, z)$	Generation function	$G_{\text{power}}/\sqrt{2\pi}/\sigma_b/E_g \cdot \exp(-(x - x_b)^2/2\sigma_b)$	
σ_b	Electron beam size		1 nm
G_{power}	Electron beam strength		20 W/cm

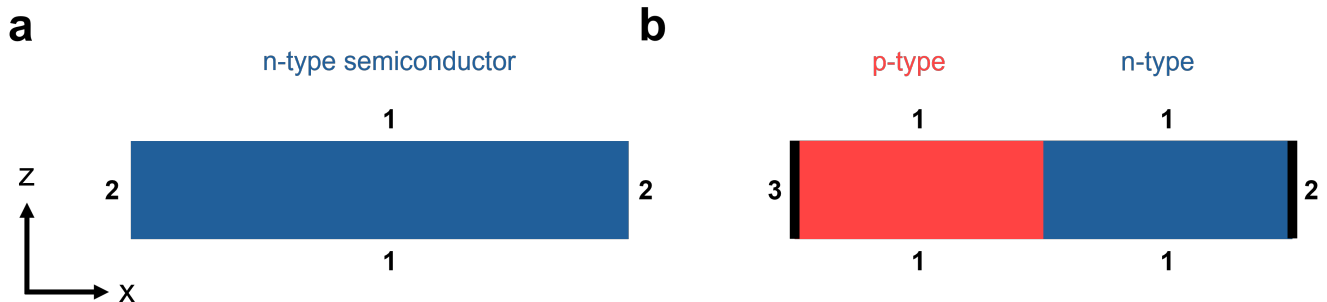


Figure S1: Boundary indices in the simulation models of the neutral n-type semiconductor (a) and the pn junction (b).

Table S2: Boundary conditions used in the FEM simulations.

Boundary index	Variable	Boundary condition type	Expression
1	Electric potential ϕ	Neumann	$\vec{n} \vec{\nabla} \phi = 0$
1	Electron concentration n	Dirichlet	$n = n_{\text{eq}}$
1	Hole concentration p	Dirichlet	$p = p_{\text{eq}}$
2	Electric potential ϕ	Dirichlet	$\phi = +V_{\text{bi}}/2$
2	Electron concentration n	Neumann	$\hat{n} \cdot D \vec{\nabla} n = s \frac{np - n_i^2}{n + n_1 + p + p_1}$
2	Hole concentration p	Neumann	$\hat{n} \cdot D \vec{\nabla} p = s \frac{np - n_i^2}{n + n_1 + p + p_1}$
3	Electric potential ϕ	Dirichlet	$\phi = -V_{\text{bi}}/2$
3	Electron concentration n	Neumann	$\hat{n} \cdot D \vec{\nabla} n = s \frac{np - n_i^2}{n + n_1 + p + p_1}$
3	Hole concentration p	Neumann	$\hat{n} \cdot D \vec{\nabla} p = s \frac{np - n_i^2}{n + n_1 + p + p_1}$

Extraction of decay lengths via exponential fits

To extract the decay length L_{decay} in excess hole concentration and STEM-EBIC profiles, least-square fits to the function

$$a \cdot \exp(-x/L_{\text{decay}}) + c$$

were performed. Special care needs to be taken that data points too close to the contact/model boundary or space charge region – with expected deviations from an exponential behavior – are excluded from the fit. In the FEM simulation, the distance of the right-most point in the fit interval to the contact/model boundary was set to 300 nm, which is well above five times the bulk diffusion length of the modeled n-type material. In the experiment, the back contact is several micrometers apart from the scanning region and no data points were excluded on the right side of the STEM-EBIC profiles. On the other hand, the left-most point was varied and for each position an exponential fit was performed to extract both a value for the decay length and its standard deviation (obtained from the covariance matrix of the least-squares parameter estimates). The typical dependence of both is plotted in combination with the corresponding STEM-EBIC profiles for simulated and experimental data in Figure S2. The value with the lowest standard deviation is chosen as the decay length as the related left-most point includes as many data points as possible, but excludes points too close to the space charge region causing an overestimation of the decay length.

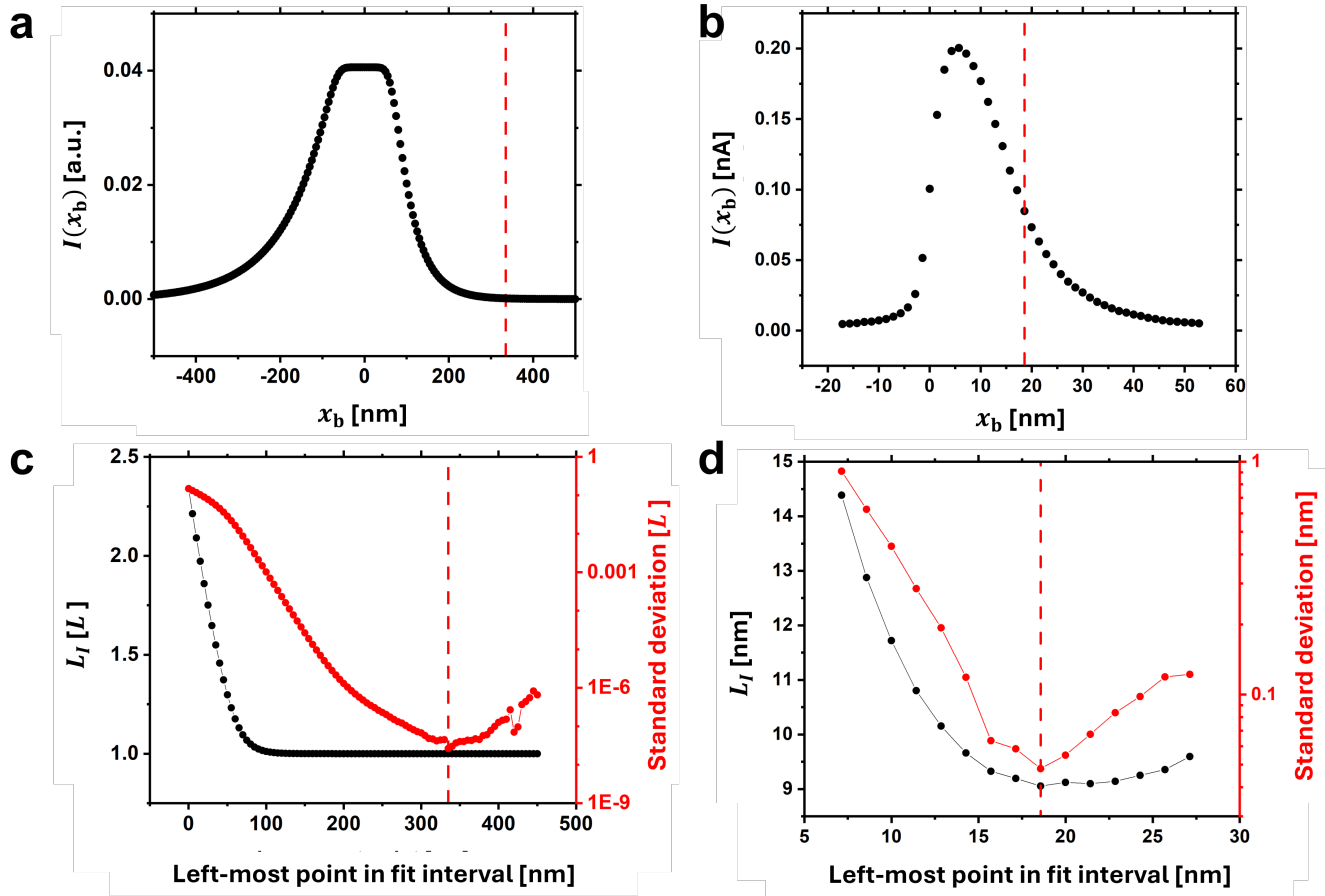


Figure S2: Examples of STEM-EBIC profiles including (a) simulated and (b) experimental data. The corresponding extracted decay length and its standard deviation obtained by an exponential fit is shown with respect to the left-most point in the fit interval in (c) and (d). The dashed red lines mark the points with minimal standard deviation and the related decay lengths were used as the values presented in the main text.

Local thickness determination

The local sample thickness was determined with EELS using the log-ratio method and a mean free path of 149.1 nm. Since the obtained values differ only by a few nanometer along the vertical direction, the thickness is evaluated along the red arrow in Figure S3a and assumed to be constant for vertical line profiles. The resulting values as a function of the horizontal position are shown in Figure S3b. The average increase in thickness corresponds to a wedge angle of 4.4° , which is close to the 5.0° rotation angle set between front and rear thinning patterns in the FIB.

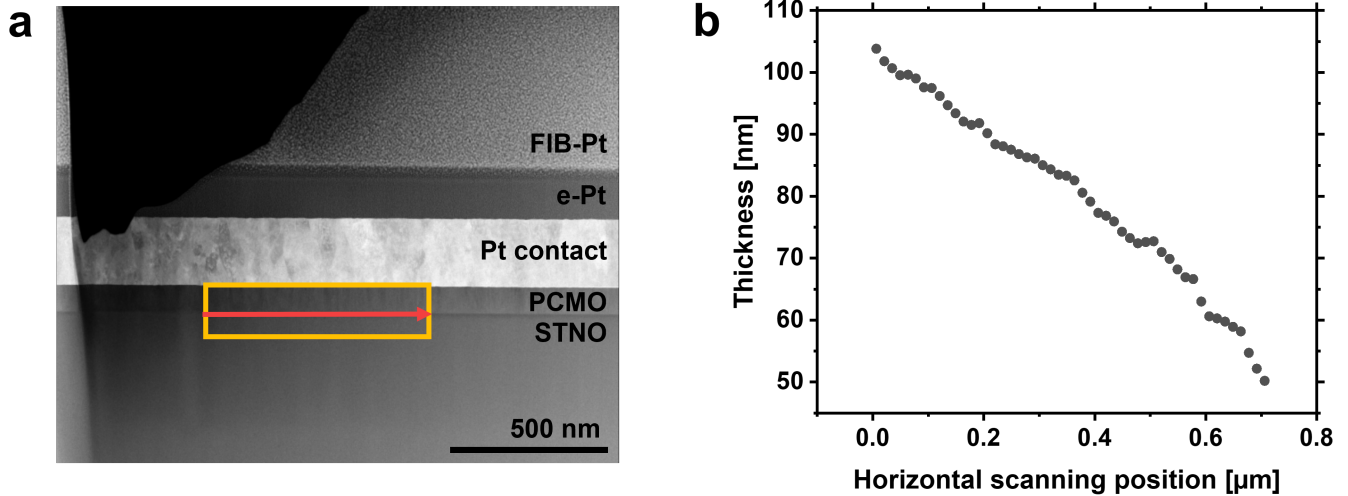


Figure S3: (a) Annular dark-field image including the experimentally investigated region of interest (yellow rectangle). The local thickness as a function of the horizontal position was extracted along the red arrow and is presented in (b).